applied optics

# Ptychography for optical metrology with limited translation knowledge

Dustin B. Moore* and James R. Fienup

Institute of Optics, University of Rochester, 275 Hutchinson Road, Rochester, New York 14627, USA
*Corresponding author: moored@secac.com

Received 7 March 2016; revised 12 May 2016; accepted 13 May 2016; posted 16 May 2016 (Doc. ID 260663); published 6 June 2016

**We introduce unknown-transverse translation diversity phase retrieval: a ptychographic algorithm for optical metrology when a subaperture is translating through a plane conjugate to the exit pupil in a very poorly known fashion. The algorithm estimates the direction of translation and the distance traveled by the subaperture from one point spread function (PSF) to the next. It also estimates unknown point target motion and rotations of the subaperture between PSF acquisitions from the PSF data.** 

***OCIS codes:*** (010.7350) Wave-front sensing; (100.5070) Phase retrieval; (120.3940) Metrology; (120.5050) Phase measurement.

http://dx.doi.org/10.1364/AO.55.004596

## 1. INTRODUCTION

Ptychography, as described in Refs. [1–5], and transverse-translation diversity phase retrieval (TTDPR), as discussed in Refs. [6–10], are techniques for inferring the unknown complex-valued field in a plane from intensity measurements collected in another plane. The unknown and measurement planes are typically connected by a propagation such as a Fraunhofer or Fresnel transform, but only certain regions of the unknown field are allowed to propagate for any particular intensity measurement. Which regions are selected is controlled by translating some feature within the unknown field or the illumination prior to it. This translating feature takes different forms, depending on the application. In coherent diffractive imaging, the unknown field is due to a coherently-illuminated transmissive object. Ptychography has been demonstrated with partially coherent illumination and with thick unknown objects where volume information is resolved, but we will consider just the coherent two-dimensional unknown case. If the coherent beam illuminates only a small region of the object, then this beam may be the feature translated; alternatively, the object may be translated through the beam. Intensities are collected for various translations of the beam, illuminating different and overlapping regions of the object. If the object is fully illuminated, a probe or subaperture with its own transmission function can be imposed before or after the object and translated instead of the illumination. Though ptychography and TTDPR algorithms solve similar mathematical problems, TTDPR uses the language of phase retrieval for wavefront sensing and the iterative nonlinear optimization of an error metric as in Refs. [11–13]. This paper utilizes the TTDPR approach to solve a wavefront sensing problem, but similar challenges would confront a ptychography algorithm that did not use nonlinear optimization.

For the optical metrology of imaging systems [7,9,10,14–16], the generalized exit pupil function [17], rather than an object, is the unknown complex field of interest. A subaperture or mask is introduced in a plane ideally conjugate to the pupil. It is translated to various overlapping regions of the pupil while point spread functions (PSFs) are collected by an array detector near a focal plane. An algorithm is applied to find the complex field consistent with all the measured PSF intensities. These algorithms include iterative transform algorithms [18] such as those derived from the ptychographic iterative engine (PIE) [1,2,4,19] and the nonlinear optimization technique of TTDPR [6–8]. If both the exit pupil function and the target being imaged by the optical system are unknown, Fourier ptychography [20,21], overlapped Fourier coding [22], or phase diversity [12] may be employed. However, for this paper, we assume the target is an unresolved target that need not be estimated.

For the simplest algorithms, both the transmission function of the subaperture or probe and the translation of that feature must be known with high accuracy [6,23]. The exact translation distance is not always exactly known, though, and often only an approximate value is available. Here we call this value, known from the design of the experiment, the prior translation estimate (PTE). In coherent diffractive imaging applications, errors in PTE can cause considerable degradation in the estimated fields [3,6,8,19,23] unless corrected. Similarly, errors in PTE degrade the accuracy of the retrieved exit pupil field in the optical metrology application. For this reason, some algorithms have the capability of refining subaperture translation estimates given the PTE and measured intensity data [5–8,24–26]. In TTDPR, a parameterized model for the exit pupil field is fit to the measured PSFs by a gradient-based nonlinear optimization algorithm [6–8]. Translation estimation is

accomplished by including the translation values in the parameters that the optimizer varies to improve the correspondence between modeled and measured PSFs [6–8]. Similarly, PIE algorithms have been developed that infer translation using gradient-free search techniques [24,25] and the serial-correlation method [5]. For some ptychography applications, the errors in PTE can be parameterized using a simplified two-parameter drift model and recovered using gradient-free optimization [26]. Gradient-based nonlinear optimization can also update the translations used in a PIE algorithm [27].

The algorithms mentioned above depend on being supplied with PTE so that they can initially approximate the unknown complex field. The PTE is used as an initial estimate for the translation. Later stages of the algorithms then refine joint estimates of the translation and the complex field using the measured intensity or PSF data. With approximately correct PTE for the initial estimate, the final result of translation estimation has been observed to be robust [5,6,8,25,27]. When the PTE becomes sufficiently inaccurate, though, simulations in [5] showed a precipitous increase in the error of translation estimation. Above some threshold in PTE error, the algorithm is unable to correct errors in the PTE and converges to incorrect translation estimates. Simulations in [27] examined this phenomenon as a function of noise in the detected intensity data and of the relative degree of overlap of the subaperture areas in neighboring translation positions. Higher signal-to-noise ratios and larger relative overlaps between subapertures delayed the onset of the precipitous increase in translation estimation error until higher PTE errors.

The existence of a precipitous increase in translation estimation errors for sufficiently imprecise PTE is consistent with our experience in optical metrology. However, the exit pupils reconstructed in the optical metrology application differ from the biological specimens examined in [5,27]. When probing the central portion of the pupil, there are few sharp-edged amplitude or phase features to act as fiducials, as is the case with coherent diffractive imaging with biological or manmade specimens that have sharp-edged features. In [16], we calculated the Cramer–Rao lower bound (CRLB) for estimating subaperture translation from the measured PSF data in the optical metrology application. Though the CRLB analysis does not indicate how accurate PTE must be for success, it does indicate situations in which there is insufficient information for a unique solution of exit pupil phase and subaperture translation.

Our interest in unknown and potentially uncorrectable translation errors comes from analyzing wavefront sensing for the Near-Infrared Camera (NIRCam) instrument on the James Webb Space Telescope (JWST). Fine-phasing of the JWST is nominally provided by focus-diverse phase retrieval using the shortwave channels of NIRCam [28]. This is not possible with the longwave channels, which lack the necessary weak lenses for defocus. They do have Lyot stops with special transmission functions intended for use in coronagraphy [29], and rotation of the pupil wheel yields a mixture of translation and rotation of the Lyot stop relative to its nominal centered position. TTDPR can be applied to a collection of PSFs acquired for various small rotations of the pupil wheel, thus achieving wavefront sensing using the longwave channel of NIRCam [10,14]. TTDPR for ground and on-orbit testing of NIRCam involves several unique challenges. For instance, calibration of the angle indication of the pupil wheel was potentially changing with each cryogenic cycling and vibration test during ground testing. Thus, the PTE available during ground testing was limited to an approximate direction of translation and an even more approximate distance. Also, the ideally unresolved point target being imaged moved in an unknown fashion from PSF to PSF for some tests. Since this target motion must be estimated and because the residual aberrations are mostly of only second radial degree, like defocus and astigmatism, translation estimation is challenging consistent with the CRLB theory and simulations in [16]. Consequently, we are concerned that systematic errors in the PTE arising from imprecise modeling of the Lyot stop motion could go uncorrected by the translation estimation steps in conventional TTDPR. We desire a TTDPR method impervious to errors in the PTE or that requires very little PTE information in a measurement situation unfavorable for estimating subaperture translation from the measured intensity data.

In this paper, we propose what we believe is a novel TTDPR algorithm called unknown transverse-translation diversity phase retrieval (UTTDPR). It avoids biases or systematic errors that might be induced by explicit translation direction or distance PTE by not utilizing such PTE. Subaperture translation values are estimated from the measured intensity data using an implicit PTE assumption that the PSFs are acquired sequentially from subaperture translations that are spatially contiguous. Initially, the algorithm solves for the exit pupil consistent with one "first" PSF. Later solutions are extended over larger and larger regions of the pupil by a multistage process that includes additional PSFs in the solution. The translation and rotation of the subaperture, the phase aberrations of the optical system, the amplitude of the exit pupil, and the motion of the point target being imaged are all estimated during solution.

The algorithm consists of two major parts: (1) an error metric involving the unknown parameters of the TTDPR measurement described in Section 2, and (2) a multistage process for minimizing the error metric that accomplishes the necessary bootstrapping process. Section 3 outlines the conventional TTDPR solution using this metric for comparison with the proposed process, described in Section 4. Experimental results from laboratory experiments are presented in Section 5.

## 2. DISCRETE MODEL AND ERROR METRIC

The UTTDPR algorithm optimizes an error metric quantifying the difference between PSFs from a parameterized model of the optical system and the actual measured PSFs. This section discusses the parameterized model for the PSF intensity and the error metric. It begins with a model for the phase and amplitude of the exit pupil of the system.

Let $\boldsymbol{Z}_j$ be a discretely sampled two-dimensional array representing the $j$th Noll-ordered Zernike polynomial function [30]. A parameterization of the phase of the exit pupil for the $k$th PSF is

$$\boldsymbol{\phi}_k = a_{2,k}\boldsymbol{Z}_2 + a_{3,k}\boldsymbol{Z}_3 + \sum_{j=4}^{J} a_j \boldsymbol{Z}_j, \tag{1}$$

where $a_{2,k}$ and $a_{3,k}$ are coefficients of the tip and tilt linear phase terms of the $k$th PSF, and $a_j$ is the $j$th Zernike polynomial coefficient for all of the PSFs for $j \geq 4$. This model allows the linear phase terms to differ between PSFs in a condition we refer to as the unshared linear phase case, which accommodates for a translating detector or a target translating within an isoplanatic patch of the optical system as outlined in [16]. If the linear phase coefficients are known to be identical for all PSFs, the model reduces to the simpler expression,

$$\boldsymbol{\phi}_k = \sum_{j=2}^{J} a_j \boldsymbol{Z}_j, \tag{2}$$

which we call the shared linear phase case and it is independent of $k$. The constant term $\boldsymbol{Z}_1$ is not included in Eqs. (1) and (2), as it is undetectable by phase retrieval.

We refer to the amplitude in the exit pupil, when the subaperture is not present, as the fixed amplitude. The fixed amplitude may include a fixed aperture stop of the system, the effects of vignetting, and other features of the pupil illumination that do not translate with the subaperture. Furthermore, we presume that the fixed amplitude must be estimated from PSF data. Earlier work [31,32] observed difficulty in estimating amplitude from near-focus PSFs without multiple planes of focus-diverse PSF data. The methods proposed in [32] improve amplitude retrieval for near-focus PSF data. However, these methods assume that the unknown amplitude is binary in nature (fully transmissive or completely opaque at each point). This assumption is appropriate for retrieving an unknown hard-edged stop in the subaperture plane. It is less suited to estimating a nonbinary, smoothly varying shading of the fixed amplitude. Amplitudes with smoothly varying features can occur when the beam is vignetted by a surface that is not in the plane of the subaperture or due to the effects of a resolved, coherently, or partially coherently illuminated target. We have observed that a fixed amplitude model parameterized by coefficients of a Zernike polynomial can retrieve both smoothly-varying and hard-edged fixed amplitudes [33]. As in [33], we here model the fixed amplitude at array pixel $[n_r, n_c]$ by

$$\boldsymbol{A}_{\mathrm{F}}[n_r, n_c] = \begin{cases} 1.0 + \boldsymbol{C}[n_r, n_c] & \text{if } \boldsymbol{C}[n_r, n_c] > -1.0 \\ 0.0 & \text{otherwise,} \end{cases} \tag{3}$$

where

$$\boldsymbol{C} = \sum_{l=2}^{L} d_l \boldsymbol{Z}_l, \tag{4}$$

and $d_l$ is the $l$th coefficient of a Zernike polynomial. The value of 1.0 in Eq. (3) is arbitrary but that value should be positive, and its negative should appear in the inequality of the if-condition. Parameterized models for the phase of an unknown field, like Eq. (2), are common in phase retrieval [11,13] but similarly parameterized amplitude models are novel. This model encompasses three useful characteristics for amplitude estimation. First, the model can vary from highly-regularized solutions when $L$ is small, to more detailed solutions, when $L$ is larger. This functionality will be used by the unknown TTDPR algorithm to avoid overfitting the model to the data in situations where there is insufficient data to constrain a fixed amplitude model with many degrees of freedom. Second, Eq. (3) prohibits negative amplitudes that would yield undesirable $\pi$-phase shifts in the resulting exit pupil model. Third, since gradient formulas exist for the parameters in Eqs. (3) and (4) despite the discontinuity imposed by Eq. (3), efficient estimation of $d_l$ can be performed jointly with the other unknowns during gradient-based optimization.

Having defined the phase and amplitude as above, a sampled array representing the field in the exit pupil absent the effects of the subaperture is

$$\boldsymbol{f}_k = \boldsymbol{A}_{\mathrm{F}} \circ \exp(i\boldsymbol{\phi}_k), \tag{5}$$

where the complex exponential function is performed element-wise and the $\circ$ operator represents the element-wise product of two arrays. The generalized exit pupil function [17] is

$$\boldsymbol{g}_k = \boldsymbol{B}_k \circ \boldsymbol{f}_k, \tag{6}$$

where the array $\boldsymbol{B}_k$ represents the transmission function of the subaperture after having been rotated by an angle $\theta_k$ and translated by a distance $(s_k, t_k)$.

Let $\boldsymbol{A}_{\mathrm{S}}$ be a sampled version of the subaperture transmission function in a reference location having zero rotation and translation. Having $\boldsymbol{A}_{\mathrm{S}}$ that is zero outside a certain bounding area lowers the detector sampling requirements [7]. This limited support also allows for overlap of the subaperture from one PSF to the next: a defining feature of ptychography that stabilizes the convergence of the phase retrieval algorithm [2]. Next, we define a model for how $\boldsymbol{B}_k$ can be calculated from $\theta_k$, $(s_k, t_k)$ and $\boldsymbol{A}_{\mathrm{S}}$. Earlier TTDPR methods [7,14], used the discrete Fourier shift theorem to evaluate translation. This was because Dirichlet kernel interpolation is effectively sinc interpolation if the arrays being interpolated are sampled finely enough to include the band limit of the continuous functions they sample. However, if $\boldsymbol{A}_{\mathrm{S}}$ is insufficiently sampled, Dirichlet kernel interpolation will make $\boldsymbol{B}_k$ an aliased representation that is beset with Gibbs ringing along and near the edges of the subaperture. The earlier work [7] avoided this issue by applying the discrete Fourier shift theorem to the field incident on the subaperture under the assumption that the field would be band limited. This assumption usually holds when the subaperture does not overlap the edge of a hard-edged aperture of the system. For the UTTDPR algorithm, however, we do not require that either the subaperture or the field impinging upon the subaperture be band-limited functions. Hence, we calculate $\boldsymbol{B}_k$ from $\boldsymbol{A}_{\mathrm{S}}$ using bilinear interpolation, as detailed in Appendix A, since it does not cause Gibbs ringing and allows inclusion of subaperture rotation in the model.

Next, consider the calculation of an array representing the field in the plane of the detector. The field in the plane of a detector near-focus is a Fraunhofer propagation [14,17]:

$$G_k(x, y) = \frac{A}{\lambda z} \iint_{-\infty}^{\infty} g_k(u, v) \exp\left[-\frac{i2\pi}{\lambda z}(xu + yv)\right] \mathrm{d}u\mathrm{d}v, \tag{7}$$

where $A$ is a constant amplitude, $\lambda$ is the wavelength of light, and $z$ is the distance between the exit pupil and detector planes. A quadratic phase terms in $x$ and $y$ has been left out of Eq. (7) since only intensity is measured, and $g_k$ is defined to include the quadratic phase in $u$ and $v$ associated with measurements not exactly at the focus plane. Let $g_k(u, v)$ be sampled in

two dimensions at intervals $\Delta_u$ to yield the $N$ by $N$ array $\boldsymbol{g}_k[n_r, n_c]$ with row and column indices $n_r$ and $n_c$, respectively, according to

$$u = \Delta_u(n_c - n_0) \quad \text{and} \quad v = \Delta_u(n_r - n_0), \tag{8}$$

where the sample at index $[n_0, n_0]$ corresponds to the optical axis where $(u, v) = (0, 0)$. Similarly, let $G_k(u, v)$ be sampled at interval $\Delta_x$ to yield an $M$ by $M$ array $\boldsymbol{G}_k[m_r, m_c]$ according to

$$x = \Delta_x(m_c - m_0) \quad \text{and} \quad y = \Delta_x(m_r - m_0), \tag{9}$$

where the index $[m_0, m_0]$ corresponds to the sample intersecting the optical axis. Substituting Eqs. (8) and (9) into Eq. (7), replacing the continuous functions with sampled equivalents and ignoring the leading constant yields

$$\boldsymbol{G}_k[m_r, m_c] = \sum_{n_r=0}^{N-1}\sum_{n_c=0}^{N-1} \boldsymbol{g}_k[n_r, n_c] \exp\{-i2\pi\alpha[(n_r - n_0) \times (m_r - m_0) + (n_c - n_0)(m_c - m_0)]\}, \tag{10}$$

where

$$\alpha = \frac{\Delta_u \Delta_x}{\lambda z}. \tag{11}$$

Equation (10) is a discrete Fourier transform (DFT) between two uniformly sampled arrays. For simplicity of the formulas and consistency with [34], we use $\alpha$ in Eq. (11) rather than the more commonly used, and inversely-proportional, term $\lambda f_{\#}/p$ defined in [35]. Such a DFT could be calculated by an operation involving zero-padding and the fast-Fourier transform (FFT) for integer values of $\alpha^{-1}$ larger than $N$ and $M$. Alternately, the chirp-Z transform can be used for general $\alpha$ [34], as can matrix multiplication [36–38]. The matrix multiplication DFT (MMDFT) is found as follows. For simplicity of the gradient calculation, let

$$\boldsymbol{\omega}[n, m] = -2.0\pi\alpha(n - n_0)(m - m_0), \tag{12}$$

for $n = 0, \ldots, N - 1$ and $m = 0, \ldots, M - 1$, and also define

$$\Omega[n, m] = \exp(i\boldsymbol{\omega}[n, m]). \tag{13}$$

Rearranging Eq. (10) as

$$\boldsymbol{G}_k[m_r, m_c] = \sum_{n_r=0}^{N} \exp[-i2\pi\alpha(n_r - n_0)(m_r - m_0)] \sum_{n_c=0}^{N} \boldsymbol{g}_k[n_r, n_c] \times \exp[-i2\pi\alpha(n_c - n_0)(m_c - m_0)], \tag{14}$$

makes it clear that the two summations are equivalent to

$$\boldsymbol{G}_k = \Omega^{\mathrm{T}} * \boldsymbol{g}_k * \Omega, \tag{15}$$

where the $*$ operator here denotes matrix multiplication.

It is often desirable to estimate $\alpha$ from the measured PSF data, since the related quantities $\Delta_x$, $\lambda$, or $z$ may not be independently known to the required precision [34,37,39]. Earlier work in estimating the related quantities used tedious grid-search techniques or gradients with respect to $\alpha$ evaluated using finite differences [39]. Later work found that the chirp-Z transform admitted analytic gradients with respect to $\alpha$ [34], thus avoiding performance impact of a grid search or a finite-differences gradient method. We find that the MMDFT similarly admits an analytic gradient with respect to $\alpha$, which is derived in Appendix B. The chirp-Z transform has better asymptotic complexity than the MMDFT [38], but we have observed that the MMDFT is computationally faster for the TTDPR problem of interest where $N$ and $M$ are too small to realize the asymptotic efficiency of the chirp-Z transform.

The predicted intensity of the $k$th PSF is given by

$$\boldsymbol{I}_k = |\boldsymbol{G}_k|^2, \tag{16}$$

where the absolute value and squaring operations are performed element-wise. Our model for the intensity measured by the detector, including an unknown detector scalar gain $\beta_k$ and bias $\gamma_k$, is

$$\boldsymbol{M}_k = \beta_k \boldsymbol{I}_k + \gamma_k \boldsymbol{1}, \tag{17}$$

where $\boldsymbol{1}$ is an $M$ by $M$ array of the value 1. Let $\boldsymbol{D}_k$ be samples of intensity of the $k$th measured PSF, and let $w_k$ be an array of weightings on the detector coordinates $[m_r, m_c]$ that are zero for samples in $\boldsymbol{D}_k$ containing bad pixels. A sum-of-squared-differences error metric between the model and measured data for the $k$th PSF is

$$E_k = \sum_{m_r, m_c} \boldsymbol{w}_k \circ (\boldsymbol{M}_k - \boldsymbol{D}_k)^2 = \sum_{m_r, m_c} \boldsymbol{w}_k \circ (\beta_k \boldsymbol{I}_k + \gamma_k \boldsymbol{1} - \boldsymbol{D}_k)^2. \tag{18}$$

As noted in [40], metrics like Eq. (18) can be minimized with respect to detector gain and bias without treating $\beta_k$ and $\gamma_k$ as unknowns in the nonlinear optimization. Closed-form solutions for the values of $\beta_k$ and $\gamma_k$ that put $E_k$ at an extremum are derived in Appendix C and listed in Eq. (C3).

Summing over the $E_k$ for individual PSFs yields a mean-squared error metric for $K$ PSFs

$$E = \sum_{k=k_{\min}}^{k_{\max}} E_k, \tag{19}$$

where $k_{\min}$ and $k_{\max}$ are the minimum and maximum index of the PSFs to be included in the error metric. Eq. (19) is implicitly a function of the unknown (1) phase parameters $a_{j,k}$, (2) amplitude parameters $d_l$, (3) subaperture translations $s_k$ and $t_k$, (4) subaperture rotations $\theta_k$, and (5) propagation scale term $\alpha$. The estimation process in the conventional and UTTDPR cases involves minimizations of the error metric in [6,7] or Eq. (19) with respect to the respective unknowns of each problem. Such nonlinear optimization may be accomplished with a gradient-based optimization such as the preconditioned conjugate-gradient method or the limited-memory Broyden–Fletcher–Goldfarb–Shanno (L-BFGS) algorithm [41,42]. However, in addition to the error metric formula, these algorithms require a method for evaluating the gradient of the error metric with respect to the unknowns. Though this gradient can be estimated by the method of finite differences, it is more efficiently and accurately estimated using an analytic gradient formula. Gradients with respect to $s_k$, $t_k$, and $\theta_k$ are evaluated in Appendix A, while the overall structure of the gradient calculation and specific gradients with respect to $a_{j,k}$, $d_l$, and $\alpha$ are provided in Appendix B.

## 3. CONVENTIONAL TTDPR

Next, we review the optimization stages of conventional TTDPR [6,7] utilizing the metric of Section 2 so that comparison may be made with the UTTDPR method discussed in

Section 4. For conventional TTDPR, it would be assumed that initial values for subaperture positions $(s_k, t_k)$ could be given by the PTE, and subaperture rotation $\theta_k$ and scaling $\alpha$ would be assumed known. Similarly, a parameterized amplitude model such as Eqs. (3) and (4) does not appear in conventional TTDPR, so it would be initially assumed that $\boldsymbol{A}_{\mathrm{F}}$ is itself approximately known. Absent specific knowledge, it may be assumed that $\boldsymbol{A}_{\mathrm{F}}$ is initially a uniform constant over a known aperture, as in [7]. Finally, the initial value of $a_{j,k}$ can be selected from many appropriate starting guesses. In many cases, the initial assumption that $a_{j,k} = 0$ (an unaberrated wavefront) will lead to successful phase retrieval. If prior knowledge of the aberrations of the system, such as an approximately known defocus or astigmatism aberration, are available, then that should be incorporated into $a_{j,k}$. Furthermore, define $J_{\mathrm{L}}$ and $J_{\mathrm{H}}$ to be two free parameters of the algorithm corresponding to the largest index of Zernike coefficient to be used during low-order and higher-order phase estimation, respectively. Exact values are problem-dependent, but we assume that $J_{\mathrm{L}} \leq J_{\mathrm{H}}$. Whichever is in use replaces the $J$ appearing in the summations in Eqs. (1) and (2). For instance, using $J_{\mathrm{L}} = 11$ allows estimation of the second and third radial-degree terms as well as the fourth radial-degree spherical aberration term during the low-order phase estimation.

One selection of steps for conventional TTDPR consistent with earlier work [7] for solving for the unknown parameters is as follows:

(1) **Linear phase estimation**. For each PSF, find the optimal translation of the model-predicted $\boldsymbol{I}_k$ such that it best matches the measured $\boldsymbol{D}_k$. This can be done using centroiding or the cross-correlation method of [43] to arbitrary precision, but 1/2 pixel is sufficient. For the unshared linear phase case, the discrete-Fourier shift theorem can then be used to infer new values of the linear $a_{2,k}$ and $a_{3,k}$ phase terms that yield such optimal shifts in the $\boldsymbol{I}_k$. In the shared linear phase case, the mean of the optimal shifts can be used to update the single available set of the linear phase terms $a_2$ and $a_3$.

(2) **Low-order phase estimation**. Let $k_{\min}$ and $k_{\max}$ be set to the minimum and maximum indices, respectively, of the available PSF data. Then, given the initial values for the parameters and newly-estimated linear phase terms from Step 1, minimize the error metric with respect to all linear phase parameters and low-order phase terms $a_j$ for $j \in [4, J_{\mathrm{L}}]$.

(3) **Phase and subaperture translation estimation**. Given the initial values for the parameters and newly estimated phase terms from Step 2, minimize the error metric with respect to the subaperture translations $(s_k, t_k)$ as well as all phase parameters $a_j$ for $j \in [4, J_{\mathrm{H}}]$. This allows for small errors in the subaperture translation estimate to be refined using the PSF data.

(4) **Amplitude, phase, and subaperture translation estimation**. If desired, add the per-pixel values of $\boldsymbol{A}_{\mathrm{F}}$ to the list of parameters allowed to be altered during optimization and optimize to find a pixel-by-pixel estimate for the amplitude of the exit pupil and jointly-optimal phase and subaperture translation parameters. This results in a joint estimate for amplitude $\boldsymbol{A}_{\mathrm{F}}$, aberration coefficients $a_{j,k}$ and subaperture translations $(s_k, t_k)$.

We have observed that this series of steps assists in alleviating stagnation of the optimization process in local minima of the error metric. In particular, Step 1 alleviates stagnation induced by the model PSF not having significant intensity overlapping regions of the measured PSF with significant intensity. Also, as noted in [16], the second and third radial degree phase aberrations have a critical role in contributing subaperture translation information to the subaperture translation estimation process. Consequently, we observe that estimating these lowest-order exit pupil phase in Step 2 prior to estimating subaperture translations in Step 3 aids successful retrieval. Finally, since estimating the pixel-by-pixel amplitude $\boldsymbol{A}_{\mathrm{F}}$ and estimating subaperture translation are both instances of estimating exit pupil amplitude, these estimations can have correlated errors. This is more noticeable when $\boldsymbol{A}_{\mathrm{F}}$ has a large number of degrees of freedom that can overfit the data and lead to stagnation of the optimization at a local minimum. For example, the optimizer may find a solution that erroneously models vignetting induced by the subaperture using erroneous values in $\boldsymbol{A}_{\mathrm{F}}$ rather than the correct adjustment to the subaperture translation. By estimating subaperture translation in Step 3 and reserving the pixel-by-pixel amplitude for Step 4, we encourage the optimization process to explain as much of the observed exit pupil amplitude with subaperture translation adjustments as possible. Then, in Step 4, pixel-by-pixel amplitude can be estimated with a reduced chance of a subaperture translation being mismodeled as a variation in $\boldsymbol{A}_{\mathrm{F}}$.

## 4. UTTDPR

In Section 1, we indicated the risks posed to joint translation and phase estimation by errors in the PTE going uncorrected in the final estimate. In this section, we outline UTTDPR, a method that is independent of prior direction-of-translation information and requires only a bound on the unknown distance of subaperture translation from one PSF to the next. Since explicit PTE in the form of approximate translation directions and distances is not used, it does not have to be reliably measured or estimated before application of the algorithm. Also, UTTDPR will not stagnate in a local minimum due to the influence of PTE errors on the convergence of the optimization. Still, the optimization may fail to converge, but such a failure cannot be induced by errors in the PTE, since explicit PTE is not utilized.

Estimating subaperture translation requires significant knowledge of the low-order exit pupil phase [16], but one cannot estimate phase without approximately knowing the subaperture translations. This circular dependence between subaperture translation and phase means that normal algorithms like those described in Section 3 are prone to stagnation during low-order phase estimation in Step 2. Simple choices for initial $s_k$ and $t_k$ usually result in the optimizer settling in a local minimum of $E$ with completely erroneous values of the unknown subaperture translations. The problem of simultaneously estimating phase and subaperture translation is acute in the unshared linear phase case, as any residual defocus or astigmatism in the exit pupil wavefront does not aid subaperture translation estimation as it would in a shared linear phase case [16]. Additionally, in UTTDPR, it is presumed that the pupil amplitude is also unknown, thus further complicating

subaperture translation estimation for the reason mentioned in Section 3.

UTTDPR addresses these challenges with a series of optimization steps similar to conventional TTDPR, but adjusted to confront the case that the exit pupil phase and the direction of subaperture translation from PSF to PSF is unknown. The distance translated is also unknown but presumed bounded. Let the PSFs be acquired in a sequential, contiguous, motion of the subaperture where the change in subaperture translation from PSF to PSF is a small fraction of the width of the subaperture. Similarly, we assume that the subaperture rotation varies by small amounts between PSFs with consecutive indices. Additionally, the fixed amplitude may be assumed unknown but approximately constant over the subaperture of at least one PSF with index $k'$ for which the subaperture rotation $\theta_{k'}$ can be guessed to within a small number of deg. Typically this would be from a PSF deriving from a subaperture location near the center of the fixed amplitude. If the index $k'$ of a PSF with such a subaperture translation and fixed amplitude situation is unknown, an arbitrarily chosen PSF appearing near the middle of the sequence may suffice.

As in conventional TTDPR, the initial values for $a_{j,k}$ are presumed using the best available prior knowledge, or equal to zero or some random starting guess in the absence of prior phase knowledge. We use the amplitude model of Eqs. (3) and (4) with initial values $d_l = 0$ which yields a constant $\boldsymbol{A}_{\mathrm{F}}$. The initial value for $\theta_{k'}$ is taken to be the guess mentioned above and the initial value of $(s_{k'}, t_{k'})$ is taken to be (0, 0). It is also presumed that $\alpha$ is known to within a few percent, and that this approximate value can be used as an initial guess. We define $L_{\mathrm{L}}$, $L_{\mathrm{M}}$ and $L_{\mathrm{H}}$, with $L_{\mathrm{L}} \le L_{\mathrm{M}} \le L_{\mathrm{H}}$, to be three additional free parameters of the algorithm corresponding to the largest index of a Zernike coefficient to be used during low-order, medium-order and higher-order amplitude coefficient estimation, respectively. The exact choice of these free parameters is problem dependent. Each of these three parameters replace the $L$ in Eq. (4) at various stages of estimation. Finally, the initial values of $k_{\min}$ and $k_{\max}$ are assigned to be $k'$, so that the error metric initially only includes the $k'$th PSF.

We have, through a process of trial-and-error, found a series of optimization steps based on the ideas of conventional TTDPR that often yields joint solutions for the UTTDPR problem given the starting estimates above. The unknowns to be found or refined are (1) phase parameters $a_{j,k}$, (2) amplitude parameters $d_l$, (3) subaperture translations $s_k$ and $t_k$, (4) subaperture rotations $\theta_k$, and the (5) propagation scale term $\alpha$. The steps are as follows:

(1) **Initial linear phase estimation**. The optimal translation of the model-predicted $\boldsymbol{I}_{k'}$ such that it best-matches the measured $\boldsymbol{D}_{k'}$ as outlined in Step 1 from conventional TTDPR in Section 3 is calculated. $a_{2,k'}$ and $a_{3,k'}$ are updated to incorporate these translations into the initial parameters.

(2) **Low-order phase estimation**. The error metric is minimized with respect to the linear phase terms $a_{2,k}$ and $a_{3,k}$, and the low-order phase terms $a_j$ for $j \in [4, J_{\mathrm{L}}]$. Since $k_{\min} = k_{\max} = k'$, only the $k'$th PSF contributes to the error metric. Thus, this step finds a low-order phase solution consistent with just the $k'$th PSF under the assumption that the subaperture is untranslated and the fixed amplitude is constant. The subaperture transmission function is the only distribution in the amplitude of the exit pupil model.

(3) **Initial amplitude estimation**. The amplitude coefficients corresponding to $d_l$ for $l \in [2, L_{\mathrm{L}}]$, in addition to the parameters estimated in Step 2, are allowed to vary during a minimization. This finds a joint solution for a few of the amplitude coefficients and the phase coefficients estimated in Step 2.

(4) **Initial rotation estimation**. $\theta_{k'}$ is added to the parameters estimated in Step 3 and minimization performed to find a joint solution for rotation of the subaperture during the $k'$th PSF and the previously estimated amplitude and phase coefficients.

(5) **Initial $\alpha$ estimation**. $\alpha$ is added to the parameters estimated in Step 4 and minimization of the error metric executed to find a joint solution for $\alpha$, $\theta_{k'}$, and the previously estimated amplitude and phase coefficients.

(6) **Include one lesser PSF**. If $k_{\min}$ can be decremented by one to yield the index of an available data PSF, this is done. Also, once decremented, values for $\theta_{k_{\min}}$, $s_{k_{\min}}$ and $t_{k_{\min}}$ are initially set equal to $\theta_{(k_{\min}+1)}$, $s_{(k_{\min}+1)}$ and $t_{(k_{\min}+1)}$. This makes the erroneous but useful first approximation that the $k_{\min}$th PSF is in the same location as the PSF with index $k_{\min} + 1$. The linear phases $a_{2,k_{\min}}$ and $a_{3,k_{\min}}$ are estimated by the correlation method outlined in Step 1 from conventional TTDPR in Section 3, assuming the approximate subaperture translation.

(7) **Include one greater PSF**. If $k_{\max}$ can be incremented by one to yield the index of an available data PSF, this is done. Also, once incremented, values for $\theta_{k_{\max}}$, $s_{k_{\max}}$ and $t_{k_{\max}}$ are initially set equal to $\theta_{(k_{\max}-1)}$, $s_{(k_{\max}-1)}$ and $t_{(k_{\max}-1)}$. The linear phases $a_{2,k_{\max}}$ and $a_{3,k_{\max}}$ are estimated by the correlation method, as in Step 6.

(8) **Subaperture translation estimation**. Optimization is performed to minimize the error metric with respect to the translation and linear phase terms corresponding to the $k_{\min}$th PSF if it was newly decremented in Step 6 and the $k_{\max}$th PSF if it was newly incremented in Step 7. Other unknowns, including the phase coefficients of 2nd radial degree and higher, are not allowed to vary during this optimization.

(9) **Rotation estimation**. Optimization is again performed with respect to the parameters estimated in Step 8 but also including subaperture rotation $\theta_{k_{\min}}$ if $k_{\min}$ was newly decremented in Step 6 and $\theta_{k_{\max}}$ if $k_{\max}$ was newly incremented in Step 7.

(10) **Medium-order amplitude refinement**. The amplitude coefficients corresponding to $d_l$ for $l \in [2, L_{\mathrm{M}}]$, in addition to the parameters estimated in Step 9, are allowed to vary during optimization.

(11) **Low-order phase refinement**. The low-order phase terms $a_j$ for $j \in [4, J_{\mathrm{L}}]$ are included in the list of parameters to optimize in addition to those in Step 10.

(12) **Refine everything but higher-order amplitude and phase**. Subaperture translation, rotation and linear phase terms for PSFs with indices from $k_{\min}$ though $k_{\max}$, as well as $\alpha$ and the parameters of Step 11 are allowed to vary during optimization.

(13) Repeat Steps 6 through 12, unless $k_{\min}$ and $k_{\max}$ correspond to the lowest and highest indexed data PSFs in the dataset.

(14) **High-order amplitude estimation**. The amplitude coefficients corresponding to $d_l$ for $l \in [2, L_{\mathrm{H}}]$, in addition

to the parameters estimated in Step 12, are allowed to vary during a minimization.

(15) **High-order phase estimation**. The error metric is minimized with respect to high-order phase terms $a_j$ for $j \in [4, J_H]$ in addition to the parameters refined in Step 14.

For UTTDPR in the shared linear phase case, several steps are modified. In Steps 1 and 2, it is $a_2$ and $a_3$ that are estimated rather than $a_{2,k'}$ and $a_{3,k'}$. The process of estimating linear phase by correlating model PSFs with data PSFs is eliminated entirely from Steps 6 and 7, and no attempt to optimize over linear phase is made in Steps 8–10. In Steps 11, 12, 14, and 15, $a_2$ and $a_3$ are included as parameters for optimization.

### A. Discussion

As the subaperture translations of the $k_{\min}$th and $k_{\max}$th PSFs optimize in Step. 8, the clear area of the subaperture overlaps regions of the exit pupil phase and fixed amplitude not accessed by the subaperture in the PSFs incorporated into the solution by earlier computations. Since the phase and fixed amplitude coefficients are held constant in Steps 6–9, these newly accessed regions of phase and amplitude are extrapolations using the phase and fixed amplitude found in earlier steps. Once this translation is approximated using the extrapolated phase and fixed amplitude, the subaperture rotation can be estimated in Step 9. Next, the amplitude and phase Zernike coefficients are refined in Steps 10 and 11, allowing the overall phase and fixed amplitude estimate to conform to the PSFs included in the solution. Then, most of the unknowns are refined in Step 12 to form a robust estimate for later iterations of Steps 6 through 12 incorporating PSFs that access additional new regions of the pupil. The process of estimating the translation for new PSFs using extrapolations from the model fitted to the old PSFs repeats until a joint solution for phase, amplitude, and subaperture translation is found, incorporating all PSFs. This cumulative process of solving larger and larger subproblems of the overall problem is unique to UTTDPR, and it enables a computation that begins without explicit PTE input. Also, in our experience, the incremental nature of this bootstrapping process aids convergence of the joint translation and pupil phase estimates to correct values. This is particularly important in the unshared linear phase case where the PSFs often contain less translation information than in the shared linear phase case [16].

We make no claim that the numerous steps of the UTTDPR algorithm above uniquely solve the problem. They were derived from practical experience accumulated through working with specific sets of simulated data, actual data collected in the laboratory, and from the NIRCam instrument. Depending on the particular problem, some steps may be omitted, transposed or aggregated with other steps to simplify the algorithm. The listed steps are, however, the ordering that we have found to be the most robust for the data coming from NIRCam and NIRCam-like laboratory experiments and simulations. Skipping some of the steps occasionally led to stagnation without finding a solution.

There is no guarantee that an acceptable solution for subaperture translations can always be obtained, even if the Cramer-Rao lower bound for translation estimation [16] is favorable. It may not be possible for Steps 6–8 to converge to a good joint estimate for the linear phase and subaperture translations from the estimates for exit pupil phase and amplitude derived from the earlier steps. Noise in the detected PSFs alters the location of global minimum of the error metric and may add new local minimums, as in [44]. It is also possible to have a PSF whose subaperture translation from its neighbor is so great that the optimizer would have to go up in error metric value before finding this better minimum of the error metric. This phenomenon yields a constraint on the minimum required overlap of the subaperture transmission function between neighboring PSFs similar to those noted in [5,27]. We have not assessed this distance, as it is likely highly dependent on particular pupil phase and fixed amplitudes.

## 5. LABORATORY EXPERIMENT

In [10], we reported results of applying algorithms essentially similar to UTTDPR to simulated data. For this paper, we report laboratory results using the UTTDPR algorithm. The aberrated optical system shown schematically in Fig. 1(a) was assembled to produce data for TTDPR. Light from a helium-neon laser ($\lambda = 632.8$ nm) was focused onto a pinhole spatial filter and then collimated by Lens I. The collimated beam then passed through a moving subaperture. A Lyot stop transmittance function [14], shown in Fig. 1(b), similar to the Lyot stop used in NIRCam, was cut into sheet metal to form a subaperture having a horizontal width of 4.6 mm. It was affixed

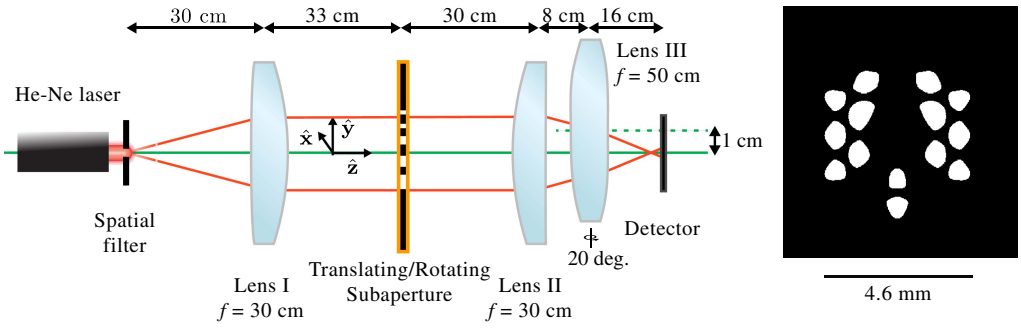


**Fig. 1.** (a) Schematic of TTDPR laboratory experiment. Not shown: neutral density filter and focusing microscope objective between the laser and the spatial filter; (b) transmission function for the subaperture.

to a rotation stage allowing it to rotate about an axis parallel to $\hat{\mathbf{z}}$. The distance from this true axis of rotation to the center of the subaperture was approximately 96 mm. The rotation stage was mounted to an X-Y translation stage. After the subaperture, the light passed through Lens II and then Lens III, which was offset in the $\hat{\mathbf{y}}$ direction and rotated about the $\hat{\mathbf{y}}$ axis by approximately 20 deg in order to induce aberrations in the imaging of the pinhole to a CCD detector having 7.4 μm square pixels. An example PSF is shown in Fig. 2(a).

In the first of two experiments performed with the apparatus, PSFs were acquired with subaperture translations on a 7-by-7 grid separated by approximately 766 μm through motion of the X-Y translation stage. Each position was randomly-perturbed by values drawn from a zero-mean Gaussian distribution having a standard deviation of 70 μm. These randomly-perturbed translations are plotted by the circle symbols in Fig. 2(b). The translation distance from one subaperture location to the next was about 17% of the width of the subaperture, a substantial overlap between neighboring positions of the subaperture. PSFs were collected sequentially down one column in $y$, then over one increment in $x$, then up the next column, and over one increment in $y$. This pattern of motions was repeated to achieve a series of PSFs arising from spatially-contiguous subaperture translations as required for UTTDPR. To simulate the effect of a moving detector or unshared linear phase in the pupil, the region of the detector pixels passed to UTTDPR was randomly offset a few pixels from one PSF acquisition to the next. This randomly offset PSF data was processed by the unshared linear-phase variant of the UTTDPR algorithm described in Section 4. The number of

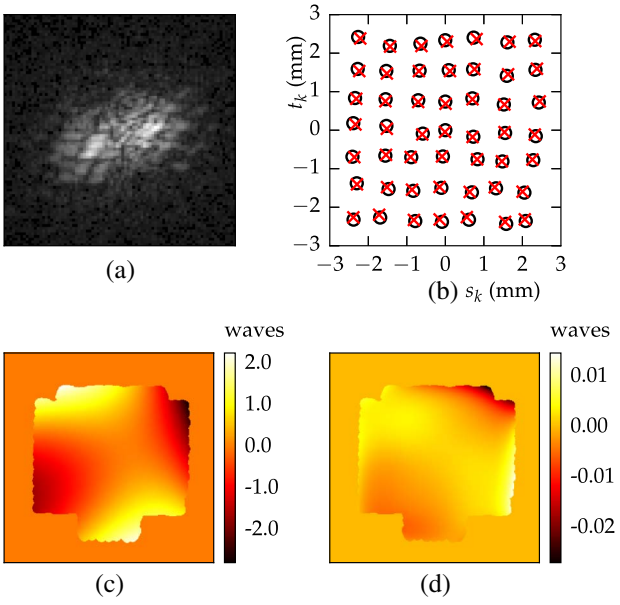


**Fig. 2.** (a) Example PSF of the aberrated system: intensity plotted to the 0.33 power; (b) scatter plot of subaperture translations for the first experiment: red × symbols are UTTDPR recovered values and black circles indicate true translations commanded to the X-Y stage; (c) retrieved pupil phase for first experiment using UTTDPR with defocus and linear phase removed; (d) phase difference (error) between UTTDPR and conventional TTDPR with knowledge of the subaperture translations for the first experiment.

Zernike phase terms were $J_{\mathrm{L}} = 9$ and $J_{\mathrm{H}} = 35$, while the number of amplitude parameters were $L_{\mathrm{L}} = 5$, $L_{\mathrm{M}} = 9$, and $L_{\mathrm{H}} = 35$. Minimization of the error metric was accomplished using the L-BFGS algorithm [41]. The algorithm had no knowledge of the specific subaperture translations, but it did have access to the approximate values of defocus phase, subaperture rotation of the initial PSF, and $\alpha$ to use as initial estimates for optimization. The subaperture translations retrieved are shown by the × symbols in Fig. 2(b). The error between the TTDPR-estimated subaperture translations and the truth from the X-Y stage had 36 μm root mean squared error (RMSE). After normalization by the reference translation amounts, the normalized root mean squared error (NRMSE) was 0.024. This error was about 0.8% of the width of the subaperture, or 0.2% of the width of the entire retrieved pupil. The pupil phase retrieved by UTDDPR is shown in Fig. 2(c), with the linear phase terms and 4.6 waves peak-to-valley (P-V) of defocus subtracted. Over regions of the pupil encompassed by any particular subaperture translation, the amount of defocus was approximately 0.5 waves P-V.

Since for these experiments we actually had good knowledge of the translations, conventional TTDPR that used this PTE was performed on the same data but without the random shifting of readout of the detector pixels. This permitted the use of shared linear phase conventional TTDPR, which is known to increase subaperture translation estimation accuracy in the presence of defocus and astigmatism [16]. Subaperture translations and rotations were estimated using conventional TTDPR given the prior translation estimate (PTE) of the reliable X-Y stage motion. The translations retrieved using conventional TTDPR were used to fit an unknown rotation between the CCD camera and the axes of subaperture motion. The truth translation position shown in Fig. 2(b) and our RMSE and NRMSEs for UTTDPR are reported relative to this rotation correction. The difference between the UTTDPR phase and conventional TTDPR reference phase is shown in Fig. 2(d) and had an average error of $3.7 \times 10^{-3}$ waves RMSE over the accessed regions of the pupil.

For the second experiment, we chose a circular motion similar to the motion of the Lyot stop about the axis of the pupil wheel in NIRCam. The transmissive parts of the Lyot stop pattern shown in Fig. 1(b) swept through the regions of the pupil shown in Fig. 3(a). To accomplish this sweeping motion with the apparatus, the rotation stage rotated from –4 to +4 deg in evenly-spaced increments to yield a motion of the center of the subaperture represented by the circle symbols in Fig. 3(b). These positions are approximate, due to the practical difficulty of estimating the lever-arm vector between the axis of rotation and the subaperture as projected into the plane perpendicular to the beam. Our best estimate for the location of the pivot point is $(s, t) = (41.5, -74.4)$ mm. The average distance translated by the subaperture from one PSF to the next was about 11% of the width of the subaperture.

A hard-edged circular aperture was imposed into the collimated space between the subaperture and Lens II to make the second experiment more representative of TTDPR with NIRCam, which may include unknown pupil-shear and vignetting. The effect of this additional aperture was to

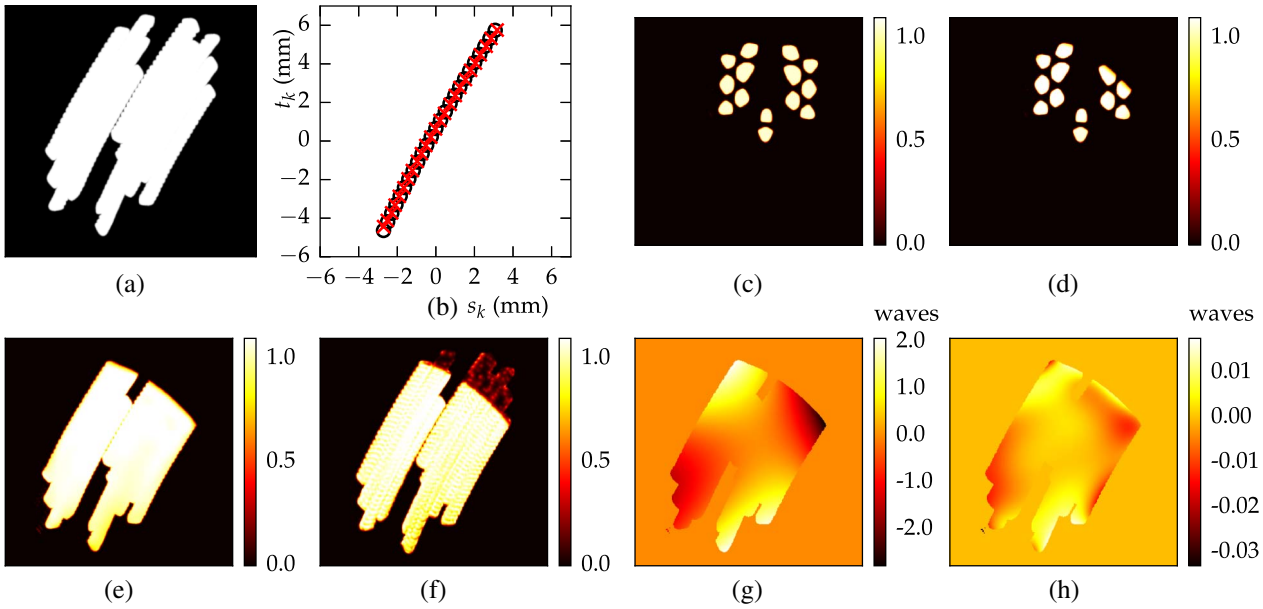


**Fig. 3.** (a) Areas of pupil accessed during subaperture motion in the second experiment; (b) scatter plot of subaperture translations for the second experiment: red × symbols are UTTDPR-recovered values and black circles indicate true translations estimated from knowledge of rotation angle and geometry; (c) subaperture transmission function for the $k = 20$th PSF, $\boldsymbol{B}_{20}$, recovered by UTTDPR and shown to the 0.5 power; (d) amplitude of the generalized pupil function for the $k = 20$th PSF, $|\boldsymbol{g}_{20}|$, recovered by UTTDPR and shown to the 0.5 power; (e) fixed amplitude to the 0.5 power recovered by UTTDPR for the second experiment; (f) fixed amplitude to the 0.5 power recovered by sieve amplitude TTDPR for the second experiment; (g) retrieved pupil phase for the second experiment using UTTDPR with defocus and linear phase removed; (h) phase difference (error) between UTTDPR and sieve amplitude TTDPR for the second experiment.

completely extinguish the beam along the upper-right corner of the pupil shown in Fig. 3(a). This unknown fixed-amplitude effect allowed the second experiment to demonstrate the fixed amplitude retrieval capability of UTTDPR in a challenging situation.

Like the first experiment, the PSF data from the second was processed by the unshared linear-phase variant of the UTTDPR algorithm, but with the number of amplitude parameters $L_{\mathrm{M}} = 20$ and $L_{\mathrm{H}} = 119$. Since $L_{\mathrm{H}}$ was much larger than $L_{\mathrm{M}}$, Step 14 was amended to include additional optimizations with 35, 54, 77, and 91 amplitude terms before finally optimizing with $L_{\mathrm{H}}$. Again, the UTTDPR algorithm had no knowledge of the specific subaperture translations in each PSF or knowledge that the subaperture motion lay on a circular arc. It only had access to approximate values of defocus phase, $\alpha$, and an intelligent guess for the rotation of the $k'$th PSF to use as starting points. The subaperture translations retrieved by UTTDPR are shown by the × symbols in Fig. 3(b). Each translation corresponds to a translated and rotated subaperture transmission function $\boldsymbol{B}_k$. One such transmission function for the 20th PSF, $\boldsymbol{B}_{20}$, is shown in Fig. 3(c).

Relative to our estimate for the true translations, the UTTDPR retrieved translations have an RMSE of 45 μm or NRMSE of 0.017. As a fraction of the width of the accessed regions of the pupil, this represents a translation estimation error of 0.3%. A portion of these translations errors are consistent with the pivot point of the rotation not being where we estimated it to be. A best-fit to the UTTDPR translations suggests motion about a pivot point of $(s, t) = (42.2, -73.9)$ mm, which was 0.88 mm away from our estimate. If we take this pivot point estimated from the UTTDPR translations as correct, the residual error of the UTTDPR solution is 37 μm RMSE, which is consistent with the 35 μm RMSE observed for the first experiment. As a fraction of the width of the overall accessed region of the pupil, this represents a 0.24% translation error.

With UTTDPR, we retrieved variations in the fixed amplitude due to the imposed circular hard-edged aperture. Fig. 3(d) shows the amplitude of the generalized exit pupil function, $|\boldsymbol{g}_{20}|$, for the example PSF having $k = 20$. It can be compared with Fig. 3(c), which shows the subaperture's contribution to the pupil amplitude without the fixed amplitude. Given this single PSF, only a portion of the retrieved fixed amplitude can be examined, but the upper-right corner indicates retrieval of a sharp-edged vignetting. The entire fixed amplitude retrieved by UTTDPR is shown in Fig. 3(e). Since the amplitude is known only in regions of the pupil covered by transmissive portions of the subaperture, the fixed amplitude is shown over the regions indicated in Fig. 3(a). Comparing that amplitude with Fig. 3(a) indicates that UTTDPR has retrieved a sharp-edged vignetting feature in the upper-right corner of the fixed amplitude consistent with the unknown aperture we imposed. It is remarkable that 119 Zernike polynomial coefficients can, in conjunction with the thresholding of Eq. (3), represent a hard-edged vignetting surface. This capability was also observed by the simulations in [33].

Since for this experiment we also had good knowledge of the translations, classic TDDPR was performed using our best

estimates for the subaperture motion. The amplitude of the fixed pupil, $\boldsymbol{A}_{\mathrm{F}}$, was allowed to vary in a pixel-by-pixel manner, as in classic TTDPR, to recover the fixed pupil effects of the additional hard-edged aperture. However, the resulting estimates for pupil amplitude were corrupted by salt-and-pepper noise to an unacceptable extent, as in [33]. We have found this failure mode to be typical of pixel-by-pixel amplitude retrieval involving a single plane very near focus, and other work has encountered similar challenges, as mentioned in Section 2. The experiment had little defocus to approximate the NIRCam application, where amplitude retrieval is challenging, and to demonstrate the capabilities of UTTDPR utilizing the Zernike amplitude model.

To generate a reference more suitable for comparison with UTTDPR, we amended our conventional TTDPR algorithm to use the method of sieves [45] to regularize the retrieved pixel-by-pixel fixed amplitude. We refer to this modified conventional TTDPR algorithm as sieves-amplitude TTDPR. It begins with performing conventional TTDPR with the starting guess that $\boldsymbol{A}_{\mathrm{F}}[n_r, n_c] = 1.0$ and allowing the pixels to vary on the interval $\boldsymbol{A}_{\mathrm{F}}[n_r, n_c] \geq 0.0$. The resulting estimate for $\boldsymbol{A}_{\mathrm{F}}$ was blurred with a wide Gaussian kernel and then used as the starting point for a second conventional TTDPR optimization. This cycle of blurring and optimization was repeated with Gaussian kernels of ever-decreasing widths to find the retrieved amplitude shown in Fig. 3(f). This amplitude also showed a hard-edged circular vignetting surface in the same place as the UTTDPR solution. However, it also showed many pixels with amplitudes between 0.1 and 0.3 in the area beyond the edge that should be near zero. Conventional TTDPR without the method of sieves also yielded significant values in the region that should be zero. We regard this as a limitation of pixel-by-pixel amplitude models, like those used in conventional TTDPR and sieves-amplitude TTDPR, because the circular aperture imposed was utterly opaque. The UTTDPR fixed-amplitude solution shows no such feature; the values of $\boldsymbol{A}_{\mathrm{F}}$ from the Zernike coefficient model in the retrieval were exactly zero in the vignetted regions beyond the circular edge. Similarly, the UTTDPR amplitude in Fig. 3(e) was smooth in the evenly illuminated regions of the pupil, while the conventional TTDPR solution had spurious fine features near the Lyot stop's edges in each of the PSFs. We attribute these fine features to artifacts of the pixel-by-pixel amplitude model that are excluded by the Zernike amplitude model used in UTTDPR. Both the UTTDPR and sieve- amplitude TTDPR amplitudes showed a darkening of the amplitude at the bottom of the displayed pupil. This was consistent with the pupil illumination due to a coherently illuminated resolved pinhole. It may be possible to construct a UTTDPR-like algorithm with a different amplitude model than the Zernike polynomial model. However, we have found the smooth amplitude extrapolations yielded by the Zernike model useful for improving the probability of convergence of UTTDPR, and we do not know which alternate amplitude models will yield a similar benefit.

The phase retrieved by UTTDPR is shown in Fig. 1(g) with 7.7 waves P-V of defocus subtracted. It was plotted over the regions of the pupil that UTTDPR indicates has an amplitude greater than 0.01. This retrieved phase was consistent with an extension of the aberrations retrieved from the first experiment shown in Fig. 1(c) extended over a larger area of the pupil, as expected. The difference between the UTTDPR phase and the sieve-amplitude TTDPR phase is shown in Fig. 3(h). The magnitude of this error was $3.0 \times 10^{-3}$ waves RMSE over the accessed regions of the pupil.

## 6. SUMMARY AND CONCLUSION

TTDPR, also known as ptychography, is a technique that can infer the complex-valued exit pupil of an optical system from PSFs of that system. The PSFs differ according to the translation of a subaperture placed in a plane approximately conjugate to the exit pupil. Algorithms can find a complex exit pupil field consistent with the measured PSF data, though they are sensitive to errors in prior knowledge of the translation of the subaperture for each PSF, which we term the PTE. Algorithms like [5–7,24,25] refine estimates of the translation using the measured PSF data, given approximately correct PTE.

These previous forms of ptychography have assumed some approximate knowledge of where the subaperture or probe is relative to the ensemble of intensity measurements. We consider optical metrology when this explicit PTE is unavailable or untrusted due to the potential for introducing systematic error. Instead, we presume a sequence of PSFs is acquired from spatially-contiguous subaperture translations in an unknown arrangement in the exit pupil, which is a very weak form of PTE. Our optical metrology technique, UTTDPR, uses the error metric of Section 2 and a multistage bootstrapping process, described in Section 4. The exit pupil phase and amplitude are initially estimated from phase retrieval performed on a single "initial" PSF. These subaperture positions in neighboring PSFs include regions of the complex exit pupil unknown to the algorithm given the phase retrieval of the first PSF. In these unknown regions, models for the complex exit pupil provide values for phase and amplitude that are extrapolations of the phase and amplitude retrieved from the single PSF. A novel amplitude model based on Zernike polynomials aided this extrapolation and the estimation of pupil amplitude. If the unknown subaperture translations of neighboring PSFs keep the subaperture inside the region of validity of the extrapolated exit pupil, acceptable subaperture translation estimates can usually be obtained by assuming the extrapolated exit pupil. Later steps find a joint phase, amplitude, and subaperture translation solution across all three PSFs and the extrapolation is eliminated using the newly included PSF data. This process of extrapolation, translation estimation, and refinement is repeated using additional PSFs not previously included in the solution until all the PSFs are part of a joint solution. The UTTDPR algorithm also simultaneously estimated: (1) a moving point target or unknown varying linear phase in the exit pupil, (2) unknown subaperture rotation, and (3) unknown scale factor inherent in the propagation from the generalized exit pupil function to the PSF plane. This estimation employed a new gradient formula for the scale term in the matrix-multiply DFT, and estimation of subaperture rotation and translation used the gradients of bilinear interpolation described in Appendix A. That appendix

also shows how gradients for geometry parameters of arbitrary resamplings involving bilinear interpolation can be found.

In Section 5, we demonstrated UTTDPR using two simple laboratory experiments with a NIRCam-like subaperture and simulated unknown point target motion. In both experiments, UTTDPR recovered the unknown subaperture translations despite the target motion and without specific knowledge of the translation of the subaperture in each PSF. In the first experiment, the subaperture was raster-scanned in two dimensions; while in the second experiment, the subaperture translated along an arc while rotating in a way similar to the Lyot stop of NIRCam. The retrieved subaperture translations had RMSEs of 0.2% and 0.3% of the width of the overall pupil for the first and second experiments, respectively. We compared the UTTDPR phase retrieval results to classic TTDPR, assuming a fixed target and known subaperture translation. UTDDPR yielded exit pupil phase errors of $3.7 \times 10^{-3}$ and $3.0 \times 10^{-3}$ waves RMSE for the first and second experiments, respectively, relative to classic TTDPR. Further, the second experiment demonstrated that UTTDPR could reconstruct the fixed amplitude due to an unknown hard-edged aperture imposed in the system. Its reconstruction using the special Zernike amplitude model was superior to that of conventional TTDPR involving a pixel-by-pixel fixed amplitude model regularized by the method of sieves.

This algorithm assumed that the target being imaged was an unresolved point, and that requirement may be impractical in some applications of interest like microscopy. We hope that future work results in similar algorithms that can be applied when the target itself is also unknown. However, we expect that the Zernike amplitude model will be insufficient to describe the pupil illumination due to an arbitrary extended target. Such an algorithm would be useful for relaxing alignment precision requirements in Fourier ptychography [20,21], and overlapped Fourier coding [22].

In conclusion, we have proposed and demonstrated an extremely flexible TTDPR algorithm for ptychographic optical metrology of imaging systems. Unlike earlier algorithms, the algorithm does not need to know the approximate translation of the subaperture relative to the ensemble of subaperture translations, nor an approximate direction of translation from one PSF to the next. In the cases evaluated, the algorithm recovered the subaperture translations and rotations from the PSF data. It simultaneously estimated significant nuisance parameters such as: (1) an unknown fixed pupil amplitude involving hard-edged features, (2) the arbitrary motion of the point target, and (3) the scale factor associated with the propagation from the aperture stop to PSF plane.

Portions of this research were presented in [10,46].

## APPENDIX A: BILINEAR INTERPOLATION

This appendix describes the bilinear interpolation of an array $\boldsymbol{A}_S$ to calculate the translated and rotated array, $\boldsymbol{B}_k$, used in Eq. (6). This description is structured to allow for an analytic gradient formula with respect to the angle of rotation and translation distances applied by the interpolation.

First, consider the mapping of physical coordinates $(u', v')$ of $\boldsymbol{A}_S$ to physical coordinates $(u, v)$ of $\boldsymbol{B}_k$ due to a rotation about the origin by angle $\theta_k$ followed by a translation. Let the translation be by a vector $[s_k, t_k]$ having units of pixels of $\boldsymbol{A}_S$. In physical coordinates, this translation is by a vector $(\Delta_u s_k, \Delta_u t_k)$, where $\Delta_u$ is the pupil sampling spacing defined in Section 2. The mapping can be represented by the matrix multiplication [47]:

$$\begin{bmatrix} u \\ v \\ 1 \end{bmatrix} = \begin{bmatrix} C_k & S_k & \Delta_u s_k \\ -S_k & C_k & \Delta_u t_k \\ 0 & 0 & 1 \end{bmatrix} * \begin{bmatrix} u' \\ v' \\ 1 \end{bmatrix}, \tag{A1}$$

where $C_k = \cos\theta_k$ and $S_k = \sin\theta_k$. An inverse mapping [47] can be found for Eq. (A1) by matrix inversion:

$$\begin{bmatrix} u' \\ v' \\ 1 \end{bmatrix} = \begin{bmatrix} C_k & -S_k & -C_k\Delta_u s_k + S_k\Delta_u t_k \\ S_k & C_k & -S_k\Delta_u s_k - C_k\Delta_u t_k \\ 0 & 0 & 1 \end{bmatrix} * \begin{bmatrix} u \\ v \\ 1 \end{bmatrix}. \tag{A2}$$

Next, we find the inverse mapping of integer sample coordinates $[n_r, n_c]$ in $\boldsymbol{B}_k$ to noninteger sample coordinates $[n_r', n_c']$ in the array $\boldsymbol{A}_S$ as required for bilinear interpolation [47]. Assume that the sample of $\boldsymbol{B}_k$ corresponding to the physical origin is at index $[n_0, n_0]$ and that $(u, v)$ can be found from $[n_r, n_c]$ by Eq. (8). Similarly let

$$u' = \Delta_u(n_c' - n_0') \quad \text{and} \quad v' = \Delta_u(n_r' - n_0'), \tag{A3}$$

where $[n_0', n_0']$ is the index of the sample corresponding to the physical origin in $\boldsymbol{A}_S$. Substituting Eqs. (8) and (A3) into Eq. (A2) and simplifying yields

$$\begin{bmatrix} n_c' & n_r' & 1.0 \end{bmatrix}^{\mathrm{T}} = \boldsymbol{R}_k^{-1} * \begin{bmatrix} n_c & n_r & 1.0 \end{bmatrix}^{\mathrm{T}}, \tag{A4}$$

where

$$\boldsymbol{R}_k^{-1} = \begin{bmatrix} C_k & -S_k & n_0' - C_k(s_k + n_0) + S_k(t_k + n_0) \\ S_k & C_k & n_0' - S_k(s_k + n_0) - C_k(t_k + n_0) \\ 0 & 0 & 1 \end{bmatrix}. \tag{A5}$$

The coordinates $n_c'$ and $n_r'$ in Eq. (A4) implicitly depend on PSF index $k$.

Let $\boldsymbol{B}_k$ have integer row and column coordinates on the interval 0 to $N - 1$. Also, let $\boldsymbol{B}_k$ be stored in linearly addressed memory in row-major order such that the linear address of a sample in memory is $n = Nn_r + n_c$. Further, let $\boldsymbol{n}$ be a 3 by $N^2$ array defined by

$$\boldsymbol{n}[\rho, n] = \begin{cases} n \bmod N & \text{for } \rho = 0 \\ \lfloor n/N \rfloor & \text{for } \rho = 1 \\ 1.0 & \text{for } \rho = 2, \end{cases} \tag{A6}$$

where mod represents the modulo operator and $\lfloor x \rfloor$ denote rounding $x$ down to the nearest integer. Eq. (A6) defines $\boldsymbol{n}$ to have the useful property that the first two rows of the $n$th column corresponds to the row index $n_r$ and column index $n_c$ of the sample of $\boldsymbol{B}_k$ at linearly addressed memory position $n$. By Eq. (A4), then, the matrix-multiplication

$$\boldsymbol{n}_{k'} = \boldsymbol{R}_k^{-1} * \boldsymbol{n}, \tag{A7}$$

has similar useful properties. By Eq. (A4), the $n$th column of $\boldsymbol{n}'$ has $n_c'$ in the first row and $n_r'$ in the second row corresponding to the coordinate of $\boldsymbol{A}_S$ to which the $n$th linearly addressed sample of $\boldsymbol{B}_k$ is inverse-mapped.

In general, the coordinates in $\boldsymbol{n}'_k$ do not fall on the integer positions associated with samples of $\boldsymbol{A}_S$ and thus some form of interpolation must be used. For TTDPR, we prefer bilinear interpolation, as described in Section 2. Next, assume that $\boldsymbol{A}_S$ has row and column coordinates with indices on the interval 0 to $N'-1$, inclusive. For coordinates $[n_r, n_c]$ corresponding to $n$ satisfying

$$0 \le \boldsymbol{n}'_k[0,n] < N'-1 \quad \text{and} \quad 0 \le \boldsymbol{n}'_k[1,n] < N'-1, \tag{A8}$$

let

$$\begin{aligned}\boldsymbol{B}_k[n_r,n_c] = &\sum_{c=0}^{1}\sum_{d=0}^{1}\{\delta_{0,c} + (-1)^{c+1}\boldsymbol{F}_{k\downarrow}[n_r,n_c]\}\\ &\times\{\delta_{0,d} + (-1)^{d+1}\boldsymbol{F}_{k\rightarrow}[n_r,n_c]\}\\ &\times\boldsymbol{A}_S[\lfloor\boldsymbol{n}'_k[1,n]\rfloor + c, \lfloor\boldsymbol{n}'_k[0,n]\rfloor + d],\end{aligned} \tag{A9}$$

where $\delta$ is the Kronecker delta and

$$\begin{aligned}\boldsymbol{F}_{k\downarrow}[n_r,n_c] &= \boldsymbol{n}'_k[1,n] - \lfloor\boldsymbol{n}'_k[1,n]\rfloor,\\ \boldsymbol{F}_{k\rightarrow}[n_r,n_c] &= \boldsymbol{n}'_k[0,n] - \lfloor\boldsymbol{n}'_k[0,n]\rfloor.\end{aligned} \tag{A10}$$

For $[n_r, n_c]$ that does not satisfy Eq. (A8), set $\boldsymbol{B}_k[n_r, n_c]$ to 0.

Since estimation of the unknown translation and rotation of the subaperture is required, we derive the steps for accumulating the reverse mode of algorithmic differentiation (RMAD) gradient [48] of the interpolation. Let $\overline{X}$ be defined as $\partial E/\partial X$ where $E$ is defined in Eq. (19). The input to the gradient of the bilinear interpolation is the array $\overline{\boldsymbol{B}_k}$ with values $\overline{\boldsymbol{B}_k}[n_r,n_c] = \partial E/\partial\{\boldsymbol{B}_k[n_r,n_c]\}$. The first step of the gradient is finding the arrays $\overline{\boldsymbol{F}_{k\downarrow}}$ and $\overline{\boldsymbol{F}_{k\rightarrow}}$, since the dependence of $\boldsymbol{B}_k$ on $\theta_k$ and $(s_k, t_k)$ comes primarily by way of $\boldsymbol{F}_{k\downarrow}$ and $\boldsymbol{F}_{k\rightarrow}$. Evaluating the sum over $c$ in Eq. (A9) shows that $\boldsymbol{B}_k$ can be expressed in terms of an element-wise addition of two terms, one involving $\boldsymbol{F}_{k\downarrow}$ element-wise multiplied with other quantities and one not involving $\boldsymbol{F}_{k\downarrow}$ at all. Consequently, by Eqs. (47) and (49) of [48],

$$\begin{aligned}\overline{\boldsymbol{F}_{k\downarrow}}[n_r,n_c] = \overline{\boldsymbol{B}_k}[n_r,n_c]&\sum_{c=0}^{1}\sum_{d=0}^{1}\{\delta_{0,d} + (-1)^{d+1}\boldsymbol{F}_{k\rightarrow}[n_r,n_c]\}\\ &\times(-1)^{c+1}\boldsymbol{A}_S[\lfloor\boldsymbol{n}'_k[1,n]\rfloor + c, \lfloor\boldsymbol{n}'_k[0,n]\rfloor + d],\end{aligned} \tag{A11}$$

for the $[n_r, n_c]$ satisfying Eq. (A8). For the remaining $[n_r, n_c]$, $\overline{\boldsymbol{F}_{k\downarrow}}[n_r,n_c] = 0$, since for those indices $\boldsymbol{B}_k$ has no dependence on $\boldsymbol{F}_{k\downarrow}$. By a similar argument,

$$\begin{aligned}\overline{\boldsymbol{F}_{k\rightarrow}}[n_r,n_c] = \overline{\boldsymbol{B}_k}[n_r,n_c]&\sum_{c=0}^{1}\sum_{d=0}^{1}\{\delta_{0,c} + (-1)^{c+1}\boldsymbol{F}_{\downarrow}[n_r,n_c]\}\\ &\times(-1)^{d+1}\boldsymbol{A}_S[\lfloor\boldsymbol{n}'_k[1,n]\rfloor + c, \lfloor\boldsymbol{n}'_k[0,n]\rfloor + d],\end{aligned} \tag{A12}$$

and $\overline{\boldsymbol{F}_{k\rightarrow}}[n_r,n_c] = 0$ for the remaining $[n_r, n_c]$.

Evaluating the gradient of Eq. (A10) is conceptually complicated by the discontinuous nature of the derivative of the floor function when its argument is an integer. The discontinuous nature of the true derivative does not significantly affect optimization if we assume the floor functions $\lfloor\boldsymbol{n}'_k[0,n]\rfloor$ and $\lfloor\boldsymbol{n}'_k[1,n]\rfloor$ are constant for small variations of $\boldsymbol{n}'_k[0,n]$ and $\boldsymbol{n}'_k[1,n]$, respectively. Presuming $\lfloor\boldsymbol{n}'_k[0,n]\rfloor$ and $\lfloor\boldsymbol{n}'_k[1,n]\rfloor$ to be essentially constant yields a gradient rule for Eq. (A10) of

$$\overline{\boldsymbol{n}'_k}[\rho,n] = \begin{cases}\overline{\boldsymbol{F}_{k\rightarrow}}[n_r,n_c] & \text{for } \rho = 0\\ \overline{\boldsymbol{F}_{k\downarrow}}[n_r,n_c] & \text{for } \rho = 1\\ 0 & \text{for } \rho = 2,\end{cases} \tag{A13}$$

where $n_r = \lfloor n/N\rfloor$ and $n_c = n \bmod N$ as in Eq. (A6). Similarly, for the purpose of computing derivatives, we will ignore the dependence of $\boldsymbol{B}_k$ on $\theta_k$ and $(s_k, t_k)$ arising from $\lfloor\boldsymbol{n}'_k[0,n]\rfloor$ and $\lfloor\boldsymbol{n}'_k[1,n]\rfloor$ appearing explicitly in Eq. (A9).

Applying Eq. (50) in [48] to Eq. (A7) yields the gradient step

$$\overline{\boldsymbol{R}_k^{-1}} = \overline{\boldsymbol{n}'_k} * \boldsymbol{n}^{\mathrm{T}}. \tag{A14}$$

By Eq. (A5), $\boldsymbol{R}_k^{-1}$ has two explicit dependencies on $s_k$. Applying Eqs. (49) and (59) from [48] to these dependences and accumulating them yields

$$\overline{s_k} = -C_k\overline{\boldsymbol{R}_k^{-1}}[0,2] - S_k\overline{\boldsymbol{R}_k^{-1}}[1,2]. \tag{A15}$$

By a similar argument,

$$\overline{t_k} = S_k\overline{\boldsymbol{R}_k^{-1}}[0,2] - C_k\overline{\boldsymbol{R}_k^{-1}}[1,2], \tag{A16}$$

and the gradients of Eq. (A5) with respect to $C_k$ and $S_k$ are

$$\begin{aligned}\overline{C_k} &= \overline{\boldsymbol{R}^{-1}}[0,0] + \overline{\boldsymbol{R}^{-1}}[1,1] - (s_k+n_0)\overline{\boldsymbol{R}^{-1}}[0,2]\\ &\quad - (t_k+n_0)\overline{\boldsymbol{R}^{-1}}[1,2],\\ \overline{S_k} &= \overline{\boldsymbol{R}^{-1}}[1,0] - \overline{\boldsymbol{R}^{-1}}[0,1] + (t_k+n_0)\overline{\boldsymbol{R}^{-1}}[0,2]\\ &\quad - (s_k+n_0)\overline{\boldsymbol{R}^{-1}}[1,2].\end{aligned} \tag{A17}$$

We will use special notation to denote the two quantities that need to be accumulated due to $\theta_k$ appearing in the definitions of both $C_k$ and $S_k$. For simplicity, denote the contribution to $\overline{\theta_k}$ due to $C_k$'s dependence on $\theta_k$ as $\overline{\theta_k}^{(C_k)}$. The gradient rules for the sine and cosine do not appear in [48], but they can be derived from the chain rule as follows:

$$\begin{aligned}\overline{\theta_k}^{(C_k)} &= \frac{\partial E}{\partial\theta_k} = \frac{\partial E}{\partial\cos(\theta_k)}\frac{\partial\cos(\theta_k)}{\partial\theta_k}\\ &= \frac{\partial E}{\partial C_k}\frac{\partial\cos(\theta_k)}{\partial\theta_k} = \overline{C_k}(-\sin\theta_k),\end{aligned} \tag{A18}$$

and for contribution to $\overline{\theta_k}$ due to $S_k$'s dependence on $\theta_k$:

$$\begin{aligned}\overline{\theta_k}^{(S_k)} &= \frac{\partial E}{\partial\theta_k} = \frac{\partial E}{\partial\sin(\theta_k)}\frac{\partial\sin(\theta_k)}{\partial\theta_k}\\ &= \frac{\partial E}{\partial S_k}\frac{\partial\sin(\theta_k)}{\partial\theta_k} = \overline{S_k}\cos\theta_k.\end{aligned} \tag{A19}$$

Finally, since $\theta_k$ appears in both $C_k$ and $S_k$, the overall gradient for rotation is

$$\overline{\theta_k} = \overline{\theta_k}^{(C_k)} + \overline{\theta_k}^{(S_k)}. \tag{A20}$$

Though this appendix has derived equations for the gradient of interpolation with respect to just subaperture translation and rotation, it is easily adapted to estimate more general transformations of $\boldsymbol{A}_S$ including scaling and shearing. Eq. (A5) can be altered to include the geometric effects of additional parameters. The gradient propagation steps for these new transformation parameters can then be calculated from the new expression

in terms of $\overline{\boldsymbol{R}^{-1}}$. For even more general translations that do not fit the model of Eq. (A7), new formulas for $\boldsymbol{n}'$ can be found in terms of the desired geometry parameters. The gradients of these parameters can be found in terms of $\overline{\boldsymbol{n}'}$ simply by applying RMAD to the new formula.

We have not attempted to estimate $\boldsymbol{A}_\mathrm{S}$ in a UTTDPR algorithm, but, like the algorithms of [4,43], it is possible to estimate the subaperture transmission function using the metric in Section 2. The gradient term with respect to $\boldsymbol{A}_\mathrm{S}$ can be found by applying Eqs. (47), (49), and (60) in [48] to Eq. (A9). The gradient computation is listed in Algorithm 1, since it is not a one-to-one function.

**Algorithm 1:** ***Calculation of $\overline{\boldsymbol{A}_\mathrm{S}}$, the gradient with respect to subaperture transmission function. We define $+=$ to be an operator that adds the right operand to the left operand and stores the result in the left operand.***

(1) **for all** $n_r'$ **and** $n_c'$ **such that** $0 \le n_r' < N'$ **and** $0 \le n_c' < N'$ **do**
(2) $\quad\overline{\boldsymbol{A}_\mathrm{S}}[n_r', n_c'] \leftarrow 0$
(3) **for all** $n$ **such that** Eq. (A8) **is True do**
(4) $\quad$**for** $c = 0$ **to** 1 **do**
(5) $\quad\quad P \leftarrow \{\delta_{0,c} + (-1)^{c+1}\boldsymbol{F}_{k\downarrow}[n_r, n_c]\}$
(6) $\quad\quad$**for** $d = 0$ **to** 1 **do**
(7) $\quad\quad\quad Q \leftarrow \{\delta_{0,d} + (-1)^{d+1}\boldsymbol{F}_{k\rightarrow}[n_r, n_c]\}$
(8) $\quad\quad\quad \overline{\boldsymbol{A}_\mathrm{S}}[\lfloor \boldsymbol{n}_k'[1, n]\rfloor + c, \lfloor \boldsymbol{n}_k'[0, n]\rfloor + d] += PQ\overline{\boldsymbol{B}_k}[n_r, n_c]$
(9) **return** $\overline{\boldsymbol{A}_\mathrm{S}}$

## APPENDIX B: GRADIENT OF THE ERROR METRIC

In this section, we apply the rules for RMAD to find the accumulated gradient terms for the model parameters beginning with $\alpha$ from Eq. (12). First, $\overline{E} = \partial E/\partial E = 1$. Applying Eq. (47) from [48] to Eq. (19) yields $\overline{E_k} = \overline{E}$ for $k$ in the interval between $k_\mathrm{min}$ and $k_\mathrm{max}$, inclusive. For other $k$, the gradient steps need not be evaluated, as those PSFs do not contribute to the error metric. Applying Eqs. (49) and (52) from [48] to Eq. (18) produces

$$\overline{\boldsymbol{M}_k} = 2\boldsymbol{w}_k \circ (\boldsymbol{M}_k - \boldsymbol{D}_k) \circ \overline{E_k} = 2\boldsymbol{w}_k \circ (\boldsymbol{M}_k - \boldsymbol{D}_k). \tag{B1}$$

Evaluating the gradient steps for Eq. (17) yields

$$\overline{\boldsymbol{I}_k} = \beta_k\overline{\boldsymbol{M}_k}, \tag{B2}$$

by Eqs. (51) in [48] and there are no other terms despite the many appearances of $\boldsymbol{I}_k$ in the formula for $\beta_k$ and $\gamma_k$ for the reasons we describe now. The construction of Eqs. (C1) and (C2) guarantee that $\partial E_k/\partial\beta_k = 0$ and $\partial E_k/\partial\gamma_k = 0$, so $\overline{\beta_k} = 0$ and $\overline{\gamma_k} = 0$, respectively. Consequently, we need not consider gradient steps arising due to $\boldsymbol{M}_k$'s dependence on $\boldsymbol{I}_k$ through $\beta_k$ and $\gamma_k$ since these are zero by the chain rule. This simple gradient evaluation was made possible by casting the bias-independent metric as Eq. (18) rather than the result of [40], for reasons outlined in Appendix C.

By Eq. (53) in [48], the gradient step for Eq. (16) is

$$\overline{\boldsymbol{G}_k} = 2\boldsymbol{G}_k \circ \overline{\boldsymbol{I}_k}. \tag{B3}$$

Next, we have the steps unique to calculating the gradient for $\alpha$ using the MMDFT. For simplicity, define

$$\boldsymbol{h}_k = \Omega^\mathrm{T} * \boldsymbol{g}_k, \tag{B4}$$

such that Eq. (15) can be written instead as

$$\boldsymbol{G}_k = \boldsymbol{h}_k * \Omega. \tag{B5}$$

By Eq. (50) in [48], the gradient steps due to the new Eq. (B5) are

$$\overline{\boldsymbol{h}_k} = \overline{\boldsymbol{G}_k} * \Omega^\mathrm{H}, \quad \overline{\Omega}^{(\boldsymbol{G}_k)} = \boldsymbol{h}_k^\mathrm{H} * \overline{\boldsymbol{G}_k}, \tag{B6}$$

where $^\mathrm{H}$ indicates the conjugate-transpose and $\overline{\Omega}^{(\boldsymbol{G}_k)}$ is the contribution to $\overline{\Omega}$ due to the explicit appearance of $\Omega$ in Eq. (B5) using the notation introduced in Appendix A. The same matrix-gradient evaluation applied to Eq. (B4) yields

$$\overline{\Omega^\mathrm{T}}^{(\boldsymbol{h}_k)} = \overline{\boldsymbol{h}_k} * \boldsymbol{g}_k^\mathrm{H}, \quad \overline{\boldsymbol{g}_k} = \Omega^* * \overline{\boldsymbol{h}_k}, \tag{B7}$$

where $\overline{\Omega^\mathrm{T}}^{(\boldsymbol{h}_k)}$ is the contribution to the gradient due to $\Omega^\mathrm{T}$ appearing in Eq. (B4). Since the values of $\Omega$ explicitly appear in $\Omega^\mathrm{T}$, but rearranged, the gradient contribution due to these values appearing in $\boldsymbol{h}_k$ is

$$\overline{\Omega}^{(\boldsymbol{h}_k)} = [\overline{\Omega^\mathrm{T}}^{(\boldsymbol{h}_k)}]^\mathrm{T} = \boldsymbol{g}_k^* * \overline{\boldsymbol{h}}_k^\mathrm{T}. \tag{B8}$$

$\Omega$ appears twice in the model of each PSF and the individual contributions must be accumulated element-wise for all PSFs to find the overall gradient with respect to $\Omega$,

$$\overline{\Omega} = \sum_{k=k_\mathrm{min}}^{k_\mathrm{max}} \overline{\Omega}^{(\boldsymbol{G}_k)} + \overline{\Omega}^{(\boldsymbol{h}_k)}. \tag{B9}$$

By Eq. (57) in [48], the gradient step associated with Eq. (13) is

$$\overline{\boldsymbol{\omega}} = \Im\{\overline{\Omega} \circ \Omega^*\}. \tag{B10}$$

Accumulating the gradient due to appearances of $\alpha$ in Eq. (12) gives

$$\overline{\alpha} = -2\pi \sum_{n=0}^{N-1}(n - n_0) \sum_{m=0}^{M-1}(m - m_0)\overline{\boldsymbol{\omega}}[n, m]. \tag{B11}$$

This concludes the gradient steps specifically involved for the MMDFT since $\overline{\boldsymbol{g}_k}$, which is needed by all future steps, was derived in Eq. (B7).

Next, we evaluate gradients for $s_k$, $t_k$ and $\theta_k$. Assuming $\boldsymbol{B}_k$ in Eq. (6) is real, applying Eqs. (B10) and (67) in [48] to Eq. (6) yields

$$\overline{\boldsymbol{B}_k} = \Re\{\boldsymbol{f}_k^* \circ \overline{\boldsymbol{g}_k}\}, \tag{B12}$$

which is needed for calculating the gradients for $s_k$, $t_k$, and $\theta_k$ using the results of Appendix A.

The steps necessary to find the gradient with respect to $d_l$ are as follows. Beginning with Eq. (6),

$$\overline{\boldsymbol{f}_k} = \boldsymbol{B}_k \circ \overline{\boldsymbol{g}_k}. \tag{B13}$$

Applying Eqs. (B10) and (67) in [48] to Eq. (5) gives

$$\overline{\boldsymbol{A}_\mathrm{F}}^{(\boldsymbol{f}_k)} = \Re\{\exp(-i\boldsymbol{\phi}_k) \circ \overline{\boldsymbol{f}_k}\}, \tag{B14}$$

where $\overline{\boldsymbol{A}_\mathrm{F}}^{(\boldsymbol{f}_k)}$ is the contribution to $\overline{\boldsymbol{A}_\mathrm{F}}$ due to $\boldsymbol{A}_\mathrm{F}$ appearing in Eq. (5) for the $k$th PSF. Accumulating these contributions element-wise with

$$\overline{\boldsymbol{A}_\mathrm{F}} = \sum_{k=1}^{K} \overline{\boldsymbol{A}_\mathrm{F}}^{(\boldsymbol{f}_k)}, \tag{B15}$$

and evaluating the thresholding operation in Eq. (3) yields

$$\overline{\boldsymbol{C}}[n_r, n_c] = \begin{cases} \overline{\boldsymbol{A}_{\mathrm{F}}}[n_r, n_c] & \text{for } \boldsymbol{C}[n_r, n_c] > -1 \\ 0 & \text{otherwise.} \end{cases} \tag{B16}$$

Then evaluating Eq. (4) finds

$$\overline{d_l} = \sum_{n_r=0}^{N-1} \sum_{n_c=0}^{N-1} (\boldsymbol{Z}_l \circ \overline{\boldsymbol{C}})[n_r, n_c], \tag{B17}$$

by Eq. (58) in [48].

Finally, we evaluate the gradients with respect to the phase coefficients $a_{2,k}$, $a_{3,k}$, and $a_k$. By Eqs. (47) and (57) in [48], the gradient steps corresponding to Eq. (5) are

$$\overline{\boldsymbol{\phi}}^{(\boldsymbol{f}_k)} = \Im\{\boldsymbol{f}_k^* \circ \overline{\boldsymbol{f}_k}\}, \tag{B18}$$

where $\overline{\boldsymbol{\phi}}^{(\boldsymbol{f}_k)}$ is the contribution due to the appearance of $\boldsymbol{\phi}$ in $\boldsymbol{f}_k$ of the $k$th PSF. In the shared linear phase case, $\boldsymbol{\phi}_k$ has the same value in each PSF, and thus the corresponding gradient contributions can be accumulated element-wise to find

$$\overline{\boldsymbol{\phi}} = \sum_{k=1}^{K} \overline{\boldsymbol{\phi}}^{(\boldsymbol{f}_k)}, \tag{B19}$$

and then from evaluating Eq. (2) we see that

$$\overline{a_j} = \sum_{n_r=0}^{N-1} \sum_{n_c=0}^{N-1} (\boldsymbol{Z}_j \circ \overline{\boldsymbol{\phi}})[n_r, n_c], \tag{B20}$$

for $j = 2, \ldots, J$ by Eq. (58) in [48]. In the unshared linear phase case, the linearity of Eq. (1) means that $\overline{a_j}$ can still be calculated by Eq. (B20) but just for $j = 4, \ldots, J$. The gradients for the linear phase terms $\overline{a_{2,k}}$ and $\overline{a_{3,k}}$ must be calculated from the individual contributions $\overline{\boldsymbol{\phi}}_k$ according to

$$\overline{a_{j,k}} = \sum_{n_r=0}^{N-1} \sum_{n_c=0}^{N-1} (\boldsymbol{Z}_j \circ \overline{\boldsymbol{\phi}}_k)[n_r, n_c]. \tag{B21}$$

## APPENDIX C: COEFFICIENTS OF THE BIAS-INDEPENDENT METRIC

The derivation of the bias-independent metric in [40] does not include an explicit formula for both the coefficients $\beta_k$ and $\gamma_k$. We derive these coefficients in different terms than one would find by substituting the equations of [40] into one another.

For the value of $\beta_k$ that puts $E_k$ in Eq. (18) at the extremum,

$$\begin{aligned} 0 = \frac{\partial E_k}{\partial \beta_k} &= \sum_{m_r, m_c} \boldsymbol{w}_k \circ (\beta_k \boldsymbol{I}_k + \gamma_k \boldsymbol{1} - \boldsymbol{D}_k) \circ 2\boldsymbol{I}_k \\ &= 2\beta_k \langle \boldsymbol{I}_k, \boldsymbol{I}_k \rangle + 2\gamma_k \langle \boldsymbol{I}_k \rangle - 2\langle \boldsymbol{D}_k, \boldsymbol{I}_k \rangle, \end{aligned} \tag{C1}$$

where $\langle \boldsymbol{X}, \boldsymbol{Y} \rangle = \sum_{m_r, m_c} \boldsymbol{w}_k \circ \boldsymbol{X} \circ \boldsymbol{Y}$ and $\langle \boldsymbol{X} \rangle = \sum_{m_r, m_c} \boldsymbol{w}_k \circ \boldsymbol{X}$. The value that puts $\gamma_k$ at extremum is, by a similar calculation,

$$0 = \frac{\partial E_k}{\partial \beta_k} = 2\beta_k \langle \boldsymbol{I}_k \rangle + 2\gamma_k \hat{w}_k - 2\langle \boldsymbol{D}_k \rangle, \tag{C2}$$

where $\hat{w}_k = \sum_{m_r, m_c} \boldsymbol{w}_k$. Linear Eqs. (C1) and (C2) have the solution

$$\begin{aligned} \beta_k &= \frac{\hat{w}_k \langle \boldsymbol{D}_k, \boldsymbol{I}_k \rangle - \langle \boldsymbol{I}_k \rangle \langle \boldsymbol{D}_k \rangle}{\hat{w}_k \langle \boldsymbol{I}_k, \boldsymbol{I}_k \rangle - \langle \boldsymbol{I}_k \rangle^2}, \\ \gamma_k &= \frac{\langle \boldsymbol{I}_k, \boldsymbol{I}_k \rangle \langle \boldsymbol{D}_k \rangle - \langle \boldsymbol{I}_k \rangle \langle \boldsymbol{D}_k, \boldsymbol{I}_k \rangle}{\hat{w}_k \langle \boldsymbol{I}_k, \boldsymbol{I}_k \rangle - \langle \boldsymbol{I}_k \rangle^2}. \end{aligned} \tag{C3}$$

Each evaluation of $E_k$ for unique parameter values requires calculating $\langle \boldsymbol{I}_k \rangle$, $\langle \boldsymbol{D}_k, \boldsymbol{I}_k \rangle$, and $\langle \boldsymbol{I}_k, \boldsymbol{I}_k \rangle$. The values of $\langle \boldsymbol{D}_k \rangle$ and $\hat{w}_k$ only need to be evaluated once for particular $\boldsymbol{D}_k$ and $\boldsymbol{w}_k$.

**Funding.** Goddard Space Flight Center (GSFC) (NNX15AE94A).

## REFERENCES


1. H. M. L. Faulkner and J. M. Rodenburg, "A phase retrieval algorithm for shifting illumination," Appl. Phys. Lett. **85**, 4795–4797 (2004).
2. H. M. L. Faulkner and J. M. Rodenburg, "Movable aperture lensless transmission microscopy: a novel phase retrieval algorithm," Phys. Rev. Lett. **93**, 023903 (2004).
3. J. M. Rodenburg, "Ptychography and related diffractive imaging methods," Adv. Imaging Electron. Phys. **150**, 87–184 (2008).
4. A. M. Maiden and J. M. Rodenburg, "An improved ptychographical phase retrieval algorithm for diffractive imaging," Ultramicroscopy **109**, 1256–1262 (2009).
5. F. Zhang, I. Peterson, J. Vila-Comamala, A. Diaz, F. Berenguer, R. Bean, B. Chen, A. Menzel, I. K. Robinson, and J. M. Rodenburg, "Translation position determination in ptychographic coherent diffraction imaging," Opt. Express **21**, 13592–13606 (2013).
6. M. Guizar-Sicairos and J. R. Fienup, "Phase retrieval with transverse translation diversity: a nonlinear optimization approach," Opt. Express **16**, 7264–7278 (2008).
7. G. R. Brady, M. Guizar-Sicairos, and J. R. Fienup, "Optical wavefront measurement using phase retrieval with transverse translation diversity," Opt. Express **17**, 624–639 (2009).
8. M. Guizar-Sicairos and J. R. Fienup, "Measurement of coherent x-ray focused beams by phase retrieval with transverse translation diversity," Opt. Express **17**, 2670–2685 (2009).
9. M. Guizar-Sicairos, S. Narayanan, A. Stein, M. Metzler, A. R. Sandy, J. R. Fienup, and K. Evans-Lutterodt, "Measurement of hard x-ray lens wavefront aberrations using phase retrieval," Appl. Phys. Lett. **98**, 111108 (2011).
10. D. B. Moore and J. R. Fienup, "Transverse translation diversity wavefront sensing with limited position and pupil illumination knowledge," Proc. SPIE **9143**, 91434F (2014).
11. R. A. Gonsalves and R. Chidlaw, "Wavefront sensing by phase retrieval," Proc. SPIE **0207**, 32–39 (1979).
12. R. G. Paxman, T. J. Schulz, and J. R. Fienup, "Joint estimation of object and aberrations by using phase diversity," J. Opt. Soc. Am. A **9**, 1072–1085 (1992).
13. J. R. Fienup, "Phase-retrieval algorithms for a complicated optical system," Appl. Opt. **32**, 1737–1746 (1993).
14. T. P. Zielinski and J. R. Fienup, "Phase retrieval with a translating Lyot stop coronagraph mask in the JWST," in *Frontiers in Optics 2009*, OSA Technical Digest (Optical Society of America, 2009), paper SWA2.
15. H.-Y. Wang, C. Liu, S. P. Veetil, X.-C. Pan, and J.-Q. Zhu, "Measurement of the complex transmittance of large optical elements with ptychographical iterative engine," Opt. Express **22**, 2159–2166 (2014).
16. D. B. Moore and J. R. Fienup, "Subaperture translation estimation accuracy in transverse translation diversity phase retrieval," Appl. Opt. **55**, 2526–2536 (2016).
17. J. W. Goodman, *Introduction to Fourier Optics*, 3rd ed. (Roberts, 2005).
18. J. R. Fienup, "Phase retrieval algorithms: a comparison," Appl. Opt. **21**, 2758–2769 (1982).
19. F. Hüe, J. M. Rodenburg, A. M. Maiden, and P. A. Midgley, "Extended ptychography in the transmission electron microscope: possibilities and limitations," Ultramicroscopy **111**, 1117–1123 (2011).

20. Z. Bian, S. Dong, and G. Zheng, "Adaptive system correction for robust Fourier ptychographic imaging," Opt. Express **21**, 32400–32410 (2013).
21. L. Tian, X. Li, K. Ramchandran, and L. Waller, "Multiplexed coded illumination for Fourier ptychography with an LED array microscope," Biomed. Opt. Express **5**, 2376–2389 (2014).
22. R. Horstmeyer, X. Ou, J. Chung, G. Zheng, and C. Yang, "Overlapped Fourier coding for optical aberration removal," Opt. Express **22**, 24062–24080 (2014).
23. H. M. L. Faulkner and J. M. Rodenburg, "Error tolerance of an iterative phase retrieval algorithm for moveable illumination microscopy," Ultramicroscopy **103**, 153–164 (2005).
24. A. Shenfield and J. M. Rodenburg, "Evolutionary determination of experimental parameters for ptychographical imaging," J. Appl. Phys. **109**, 124510 (2011).
25. A. Maiden, M. Humphry, M. Sarahan, B. Kraus, and J. Rodenburg, "An annealing algorithm to correct positioning errors in ptychography," Ultramicroscopy **120**, 64–72 (2012).
26. M. Beckers, T. Senkbeil, T. Gorniak, K. Giewekemeyer, T. Salditt, and A. Rosenhahn, "Drift correction in ptychographic diffractive imaging," Ultramicroscopy **126**, 44–47 (2013).
27. A. Tripathi, I. McNulty, and O. G. Shpyrko, "Ptychographic overlap constraint errors and the limits of their numerical recovery using conjugate gradient descent methods," Opt. Express **22**, 1452–1466 (2014).
28. D. S. Acton, J. S. Knight, A. Contos, S. Grimaldi, J. Terry, P. Lightsey, A. Barto, B. League, B. Dean, J. S. Smith, C. Bowers, D. Aronstein, L. Feinberg, W. Hayden, T. Comeau, R. Soummer, E. Elliott, M. Perrin, and C. W. Starr, "Wavefront sensing and controls for the James Webb Space Telescope," Proc. SPIE **8442**, 84422H (2012).
29. J. E. Krist, C. A. Beichman, J. T. Trauger, M. J. Rieke, S. Somerstein, J. J. Green, S. D. Horner, J. A. Stansberry, F. Shi, M. R. Meyer, K. R. Stapelfeldt, and T. L. Roellig, "Hunting planets and observing disks with the JWST NIRCam coronagraph," Proc. SPIE **6693**, 66930H (2007).
30. R. J. Noll, "Zernike polynomials and atmospheric turbulence," J. Opt. Soc. Am. **68**, 207–211 (1967).
31. G. R. Brady and J. R. Fienup, "Nonlinear optimization algorithm for retrieving the full complex pupil function," Opt. Express **14**, 474–486 (2006).
32. S. T. Thurman, R. T. DeRosa, and J. R. Fienup, "Amplitude metrics for field retrieval with hard-edged and uniformly illuminated apertures," J. Opt. Soc. Am. A **26**, 700–709 (2009).
33. D. B. Moore and J. R. Fienup, "Wavefront sensing by phase and modal amplitude retrieval," in *Imaging and Applied Optics*, OSA Technical Digest (Optical Society of America, 2013), paper OTu1A.4.
34. A. S. Jurling and J. R. Fienup, "Phase retrieval with unknown sampling factors via the two-dimensional chirp-Z transform," J. Opt. Soc. Am. A **31**, 1904–1911 (2014).
35. R. D. Fiete, "Image quality and $\lambda fn/p$ for remote sensing systems," Opt. Eng. **38**, 1229–1240 (1999).
36. R. Soummer, L. Pueyo, A. Sivaramakrishnan, and R. J. Vanderbei, "Fast computation of Lyot-style coronagraph propagation," Opt. Express **15**, 15935–15951 (2007).
37. T. P. Zielinski, "Robust image-based wavefront sensing," Ph.D. dissertation (University of Rochester, 2011).
38. M. D. Bergkoetter, A. S. Jurling, and J. R. Fienup, "Optical propagations with arbitrary sample spacing," in *Computational Optics Sensing and Imaging*, OSA Technical Digest (Optical Society of America, 2014), paper CTh3C.1.
39. T. P. Zielinski, B. H. Dean, J. S. Smith, D. L. Aronstein, and J. R. Fienup, "Determination of the sampling factor in a phase-diverse phase retrieval algorithm," in *Frontiers in Optics*, OSA Technical Digest (Optical Society of America, 2010), paper FWJ3.
40. S. T. Thurman and J. R. Fienup, "Phase retrieval with signal bias," J. Opt. Soc. Am. A **26**, 1008–1014 (2009).
41. C. Zhu, R. H. Byrd, P. Lu, and J. Nocedal, "Algorithm 778: L-BFGS-B: Fortran subroutines for large-scale bound-constrained optimization," ACM Trans. Math. Softw. **23**, 550–560 (1997).
42. J. Nocedal and S. Wright, *Numerical Optmization* (Springer, 2006).
43. M. Guizar-Sicairos, S. T. Thurman, and J. R. Fienup, "Efficient subpixel image registration algorithms," Opt. Lett. **33**, 156–158 (2008).
44. A. C. Hurst, T. B. Edo, T. Walther, F. Sweeney, and J. M. Rodenburg, "Probe position recovery for ptychographical imaging," J. Phys. **241**, 012004 (2010).
45. W. G. Carrara, R. S. Goodman, and R. M. Majewski, *Spotlight Synthetic Aradar: Signal Processing Algorithms* (Artech House, 1995).
46. D. B. Moore and J. R. Fienup, "Sub-aperture position estimation in transverse-translation diversity wavefront sensing," in *Imaging and Applied Optics*, OSA Technical Digest (Optical Society of America, 2015), paper AOM3F.4.
47. G. Wolberg, *Digital Image Warping* (IEEE, 1990).
48. A. S. Jurling and J. R. Fienup, "Applications of algorithmic differentiation to phase retrieval algorithms," J. Opt. Soc. Am. A **31**, 1348–1359 (2014).